ACS APPLIED MATERIALS & INTERFACES

www.acsami.org

Research Article

# Effect of Nanoscale Confinement on Polymer-Infiltrated Scaffold Metal Composites

Shawn M. Maguire,[‖] Connor R. Bilchak,[‖] John S. Corsi, Samuel S. Welborn, Theresa Tsaggaris, Jamie Ford, Eric Detsi, Zahra Fakhraai,* and Russell J. Composto*

Cite This: https://doi.org/10.1021/acsami.1c12491

Read Online

ACCESS | Metrics & More | Article Recommendations | Supporting Information

**ABSTRACT:** Most research on polymer composites has focused on adding discrete inorganic nanofillers to a polymer matrix to impart properties not found in polymers alone. However, properties such as ion conductivity and mechanical reinforcement would be greatly improved if the composite exhibited an interconnected network of inorganic and polymer phases. Here, we fabricate bicontinuous polymer-infiltrated scaffold metal (PrISM) composites by infiltrating polymer into nanoporous gold (NPG) films. Polystyrene (PS) and poly(2-vinylpyridine) (P2VP) films are infiltrated into the ∼43 nm diameter NPG pores via capillary forces during thermal annealing above the polymer glass transition temperature ($T_g$). The infiltration process is characterized *in situ* using spectroscopic ellipsometry. PS and P2VP, which have different affinities for the metal scaffold, exhibit slower segmental dynamics compared to their bulk counterparts when confined within the nanopores, as measured through $T_g$. The more attractive P2VP shows a 20 °C increase in $T_g$ relative to its bulk, while PS only shows a 6 °C increase at a comparable molecular weight. The infiltrated polymer, in turn, stabilizes the gold nanopores against temporal coarsening. The broad tunability of these polymer/metal hybrids represents a unique template for designing functional network composite structures with applications ranging from flexible electronics to fuel cell membranes.

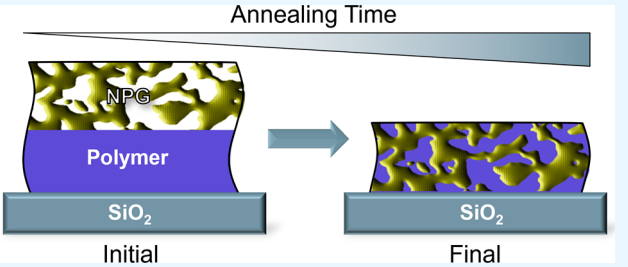


**KEYWORDS:** *glass transition, polymer, nanocomposite, nanoporous metal, confinement, polymer dynamics*

## INTRODUCTION

Polymer nanocomposites (PNCs), broadly defined as materials containing both an organic polymer phase and an inorganic nanofiller phase, have been extensively investigated for their unique properties.[1,2] PNCs have been fabricated for applications ranging from gas separations[3,4] and optical response materials[5−7] to mechanical reinforcement[8,9] and ion conduction membranes.[10] The design of functional PNC materials goes beyond identifying properties of the individual components, as the composite properties are intricately tied to the dispersion state of the nanofiller within the polymer matrix[11,12] as well as the geometry and interfacial properties, given the large number of interfaces generated.[13−15] For example, nanoparticles (NPs) can be directed to phase separate to the interfaces within polymer blends, resulting in bicontinuous structures with a quenched domain size;[16,17] NPs can also be directed toward the interfaces of self-assembled block copolymers.[18] Hore et al. have shown that nanorod aggregation can be utilized to vary absorption properties across the visible spectrum.[6,7] Kumar et al. have also shown that the storage modulus of PNCs heavily depends on the morphology of the particles and is tunable through their dispersion in the polymer phase.[19−21]

While the target application may dictate the desired PNC morphology, several applications benefit from having a percolated network of inorganic and organic phases, i.e., a bicontinuous structure. For example, the mechanical reinforcement in percolated cellulose nanofiber/polymer composites can be increased by up to 3 decades relative to the neat polymer, attributed to the connectivity of the high aspect ratio "whiskers".[22−24] Carbon nanotube networks created through selective alignment have displayed mechanical reinforcement as well as increased electrical[25,26] and thermal[27] conductivities. The impact of nanofiller percolation on polymer properties has additionally been studied in the context of developing materials with superior ionic conductivity. Maréchal et al.[28] demonstrated that the percolation of the conducting inorganic and organic hybrid aggregates significantly increased ion conduction. Percolation of the inorganic domains has also been linked to performance enhancements in dielectric[29,30] and gas diffusion[31] properties.

Typical synthetic pathways to create percolated PNCs can be challenging and rely on mixing discrete inorganic materials

Received: July 2, 2021
Accepted: August 24, 2021

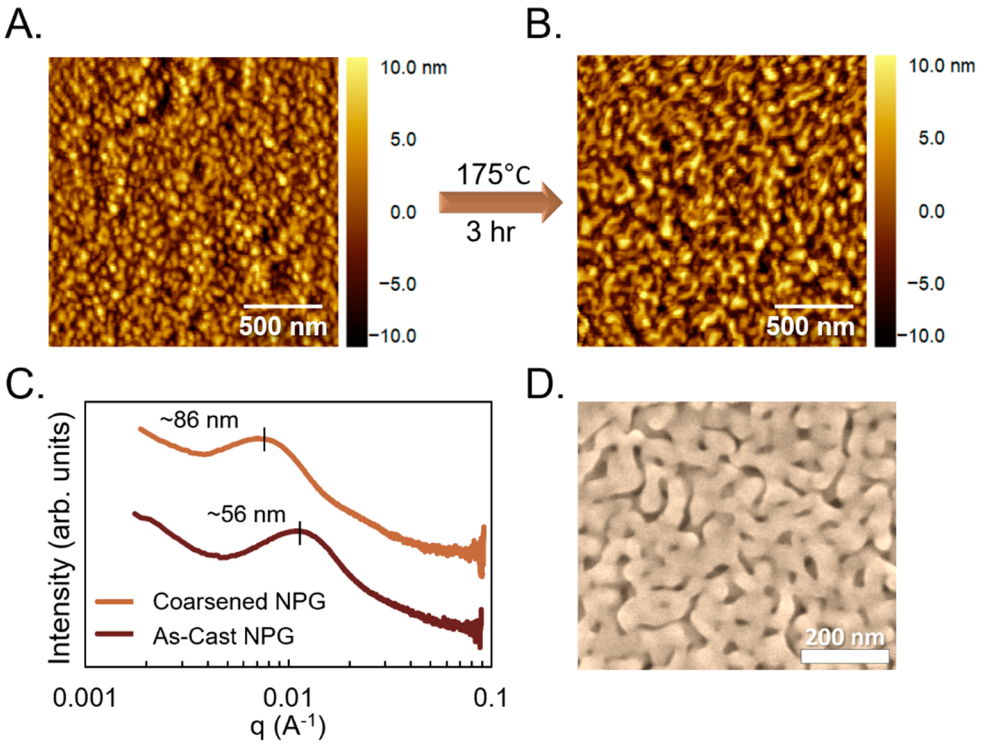


**Figure 1.** Structural characterization of NPG thin films. (A, B) AFM images (A) as-cast and (B) after coarsening at 175 °C for 3 h. The interligament distance increases by approximately 20 nm during coarsening. (C) Small-angle X-ray scattering from the as-cast and coarsened NPG. The single, broad peak corresponds to the interligament distance and correlates with AFM image analysis. The data for coarsened NPG is shifted vertically for clarity. (D) SEM image of the NPG film surface. The ligament structure is clearly visible with feature sizes comparable to AFM and SAXS.

with a polymer host. To achieve percolation, the NPs must meet one or more requirements including: (I) large size, (II) high aspect ratio, or (III) high loading (>20 vol %). However, each of these requirements presents their own challenges. For example, utilizing large NPs decreases the surface-area-to-volume ratio of the filler material, affecting their functionality. High aspect ratio NPs are generally more expensive to produce, with some notable exceptions (e.g., carbon nanotubes[25,26] and methyl cellulose[22−24]). Lastly, PNCs fabricated by loading a large volume fraction of inorganic filler into the polymer host tend to be extremely brittle and have poor NP dispersion, leading to agglomeration rather than percolation, which complicates both their fabrication and characterization.[32−34] As a result, only a few prominent examples of high-inorganic-phase loading PNCs have been demonstrated.[35,36] In these studies, PNCs were prepared through the capillary rise infiltration (CaRI) of polymers into films of randomly packed NPs, resulting in a network of nanopores whose size is set by the diameter of the NP. While directed self-assembly of the NP phase, through NP/polymer interactions[37] or via external fields,[38,39] may be an attractive method to generate percolated PNCs, these methodologies require additional processing steps and are often imperfect. The rational design of a polymer composite with percolated domains without the need of complex chemistry or laborious processing conditions thus remains an open challenge.

In this work, we fabricate and characterize a polymer-infiltrated scaffold metal (PrISM), a new class of percolated polymer nanocomposites. More specifically, we generate bicontinuous films of nanoporous metal filled with polymer. Our approach differs from previous polymer composites significantly: instead of using discrete NP materials, *we begin with an inorganic filler that is intrinsically percolated*, thereby circumventing the limitations imposed by the conventional blending approach and avoiding bottlenecks to achieving percolation. We take advantage of the extensive work on nanoporous metal synthesis and characterization demonstrating the ability to tune both the metal porosity and size distribution[40−42] as well as its electrochemical performance.[43,44] The use of this architecture for polymer composite applications is relatively nascent, with only a few studies exploring the mechanical[45−48] or electrochemical[49−51] properties of these materials. Therefore, there is a large potential for these materials as facile media to systematically design and study a wide array of percolated PNCs.

Using this novel scaffold approach, we investigate the imbibement of polystyrene (PS) and poly(2-vinylpyridine) (P2VP) into nanoporous gold (NPG) films by adapting the thermally induced capillary rise method previously described.[35,36] Here, PS and P2VP were chosen due to their relatively hydrophobic and hydrophilic nature, respectively, allowing for the investigation of changes in confinement behavior due to interactions between polymer and metal scaffold through the minimization of monomer size, backbone stiffness, and bulk glass transition effects. We show that both PS and P2VP readily infiltrate into the NPG after annealing at 150 °C for 3 h, provided that their radius of gyration ($R_g$) is less than the pore radius. In contrast, PS chains with an $R_g$ larger than the nanopore radius (i.e., $>M_w \approx 750$ kDa) infiltrate at a much slower rate and are unable to completely fill the pores without a substantial increase in temperature and imbibement time. Interestingly, at 150 °C for comparable low


https://doi.org/10.1021/acsami.1c12491
ACS Appl. Mater. Interfaces XXXX, XXX, XXX−XXX

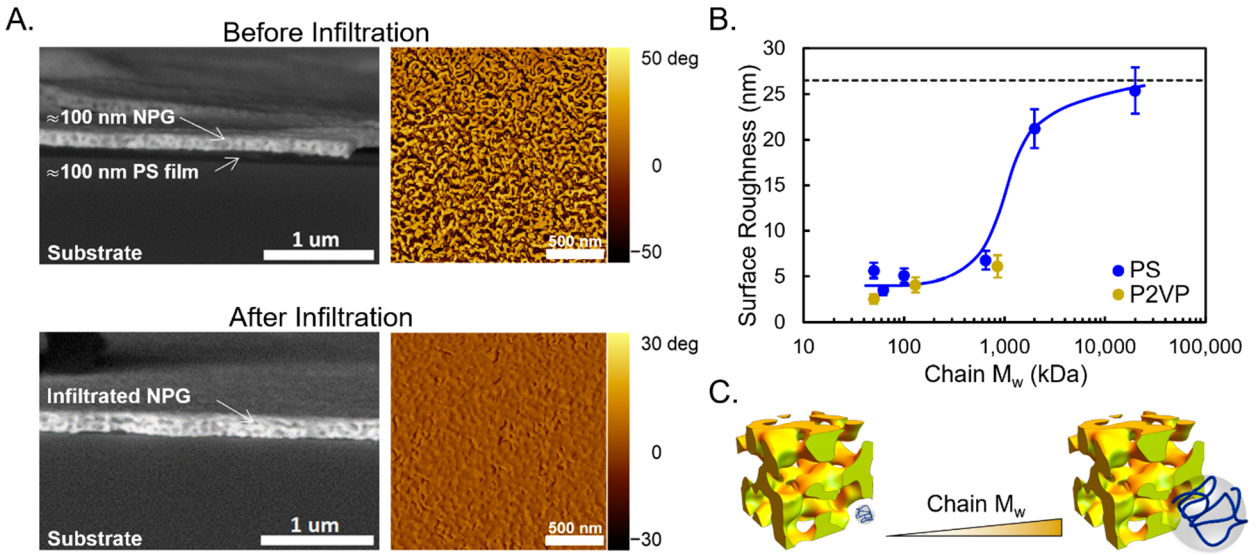


**Figure 2.** (A) Cross-sectional SEM images and AFM phase images of (top) the NPG/PS-64 bilayer before infiltration and (bottom) infiltrated NPG after annealing at 150 °C for 3 h. After annealing, the PS-64 film is not visible, and the AFM phase contrast is significantly reduced. (B) AFM root-mean-square surface roughness of the composites after infiltration as a function of molecular weight. Roughness is measured across an area of $2 \times 2\ \mu m^2$. The dashed line represents the surface roughness of as-cast NPG before polymer infiltration. (C) Schematic showing the importance of polymer chain dimension relative to the NPG pore during infiltration.

$M_w$ (ca. 50 kDa), PS is found to infiltrate the gold scaffold 10× faster than P2VP. For both PS and P2VP, the glass transition temperature ($T_g$) increases when confined in NPG. While the $T_g$ increases as much as 6 °C for PS, P2VP shows up to a 20 °C increase. This is attributed to P2VP's stronger affinity for gold than PS, which has been demonstrated in the literature to be a result of the coordination between the gold and the nitrogen atom in the pyridine group of P2VP.[18,52−54] Furthermore, whereas the unfilled NPG undergoes coarsening, the pore size of NPG infiltrated with polymer remains constant over 200 days at room temperature. This enhanced morphological stability may address an outstanding limitation when using nanoporous metals as electrodes in battery applications.

## RESULTS AND DISCUSSION

**Characterization of the Nanoporous Gold Scaffold.** We focus first on characterizing the structure of the NPG thin films. NPG films are readily fabricated by free corrosion dealloying of a ∼100-nm-thick gold/silver precursor film with composition $Au_{35}Ag_{65}$ at %. Here, nanoporosity is formed during the selective leaching of Ag from the $Au_{35}Ag_{65}$ at % alloy via a spinodal decomposition pathway (details provided in the Materials and Methods section). Recently, Detsi et al. have performed a thorough investigation of the microstructures of these nanoporous materials, including the pore size distribution, pore curvature, and specific surface area.[55] Figure 1A shows an atomic force microscopy (AFM, Agilent 5420) image of the NPG after the dealloying process, where the quasirandom structure reminiscent of spinodal decomposition is visible. Image analysis via a radial autocorrelation function using Gwyddion software (see Supporting Information) shows an average ligament−ligament spacing of 59 ± 4 nm, similar to previous observations on these materials.[55,56] Spectroscopic ellipsometry (SE, Woollam M2000) characterization of these materials (see Supporting Information) can also yield the porosity of the NPG, which we measure as 53 ± 4%. This value is in the vicinity of the atomic percent of silver in the precursor alloy film, indicating complete dealloying. From these values, we estimate the nanopores have a diameter of 0.53 × 59.0 = 29.7 nm.[55,57]

Subsequent infiltration of the polymer chains into the NPG films requires thermal annealing at temperatures well above the polymer $T_g$. Therefore, we investigated the effect of thermal annealing on the structure of the gold ligaments, which are expected to coarsen at elevated temperatures,[56−58] to determine the stability of the pore structure. Figure 1B shows an AFM image of the same NPG film after thermal annealing at 175 °C for 3 h. Here, the average ligament−ligament distance increases by approximately 25 nm during heat treatment to 81 ± 8 nm, which corresponds to a nanopore size of ∼43 nm and is consistent with results from comparable annealing procedures.[43] Measurements of the ligament−ligament distance in the as-cast and coarsened NPG films via small-angle X-ray scattering (SAXS, Xenocs Xeuss 2.0, Dual Source and Environmental X-ray Scattering facility of the Laboratory for Research on the Structure of Matter) are shown in Figure 1C. We observe a single, broad scattering feature that represents a characteristic dimension of the gold ligament structure;[55] the breadth of this feature is indicative of the dispersity in ligament size. The measured ligament−ligament distance of the as-cast (56 ± 1 nm) and coarsened (86 ± 1 nm) NPG agree with our AFM analysis. This suggests that a single gold ligament oriented perpendicular to the film surface would nearly span the film in thickness, which can be qualitatively seen via scanning electron microscopy (SEM, FEI Quanta 600, Nanoscale Characterization Facility of the Singh Center for Nanotechnology) in Figure 1D.

**Polymer Infiltration Characterization, Kinetics, and NPG Stability.** Polymers were infiltrated into the pores of the NPG by adapting the capillary rise infiltration procedure used in past work to infiltrate macromolecules into porous structures.[36,59] Herein, the NPG film was deposited over a polymer film and heated above the polymers' $T_g$ to induce infiltration via capillary forces. The initial polymer film thickness is chosen to be comparable to that of the NPG


https://doi.org/10.1021/acsami.1c12491
ACS Appl. Mater. Interfaces XXXX, XXX, XXX−XXX

film to ensure that there is enough polymer to completely fill the porous structure. Figure 2A shows cross-sectional SEM and AFM (phase) images for a bilayer of 100 nm NPG over ~100 nm PS-64 (see Table 1) before and after annealing at 150 °C for 3 h. Before infiltration (Figure 2A, top), the gold ligament structure is clearly visible on the surface of the bilayer, with no PS signature present in the AFM image. The corresponding cross-sectional image shows a dark band below the NPG, indicative of the PS layer. This layer is noticeably absent after annealing (Figure 2A, bottom), suggesting that the PS has infiltrated into the porous NPG film. Figure S21 shows a corresponding high-resolution cross-sectional SEM image after infiltration of PS-64 where the nanopores are completely filled with polymer throughout the NPG thickness.

**Table 1. Samples of Polystyrene and Poly(2-vinylpyridine) Used in This Study**

| sample | $M_w$ (kDa) | $M_w/M_n$ | $R_g$ (nm) |
|---|---|---|---|
| PS-50 | 50 | 1.06 | 6.1 |
| PS-64 | 64 | 1.05 | 6.7 |
| PS-106 | 106 | 1.06 | 9.0 |
| PS-650 | 650 | 1.06 | 22.1 |
| PS-2000 | 2000 | 1.30 | 38.7 |
| PS-20000 | 20 000 | 1.20 | 122.5 |
| P2VP-50 | 50 | 1.02 | 7.0 |
| P2VP-130 | 130 | 1.07 | 22.7 |
| P2VP-850 | 850 | 1.10 | 70.3 |

Surface roughness was quantified by analyzing the AFM height images of the annealed films and used to determine whether the NPG is fully infiltrated with polymer (see Supporting Information). Before complete infiltration, the NPG films have a high surface roughness, as the AFM probe only interacts with the gold ligaments. As polymer infiltrates from the bottom of the NPG, fills the inner pores, and then reaches the surface of the NPG to fill the surface pores, the roughness decreases and approaches a constant value as detected via AFM. For infiltration of PS and P2VP with molecular weights ($M_w$) from 50 to 20 000 kDa, Figure 2B shows that the surface roughness increases after 3 h of annealing at 150 °C. Below 650 kDa, the surface roughness is relatively small (ca. 5 nm), which is consistent with complete polymer infiltration within 3 h. However, under the same annealing conditions, larger molecules are unable to fully infiltrate the NPG and reach the surface, resulting in a large roughness value comparable to that of the unfilled NPG (ca. 26 nm).

We attribute the strong dependence of infiltration time on molecular weight in part to the size of the nanopore relative to that of the polymers' $R_g$. Here, this ratio is described by $L_{pore}/2R_g$, where $L_{pore}$ is the diameter of a single nanopore (ca. 43 nm). This ratio is comparable to those previously used to investigate the transport of dilute polymer chains through cylindrical pores.[46] Figure 2B suggests that chains with $2R_g < L_{pore}$ readily infiltrate into the pores, while chains larger than this critical size will be highly confined and infiltrate slower under the same annealing conditions. For our system, the polymer molecular weight corresponding to $2R_g = L_{pore}$ is ~750 kDa, which correlates well with the experimentally observed transition, in which chains larger than this $M_w$ are unable to fully infiltrate the NPG for the experimental conditions investigated.

Here, it is useful to compare (I) the characteristic time required for an unconfined polymer chain to diffuse via reptation a distance equal to the thickness of the NPG film (ca. 100 nm) and (II) how this time scale compares with whether chains of a given molecular weight have fully infiltrated into NPG after 3 h of annealing. Here, the diffusion time scales as $\sim l^2/D$, where $D$ is the polymer diffusion coefficient and $l$ is the film thickness (note: the tortuosity of the pores is neglected in this analysis). Using reptation theory and diffusion coefficients of PS chains obtained by Kramer et al.,[60] a theoretical analysis indicates that only chains with $M_w < 200$ kDa should be able to fully infiltrate. However, our data indicates that chains with $M_w$ as high as ~650 kDa fully infiltrate the NPG film. Further experiments also show that 2000 and 20 000 kDa polymers can infiltrate given longer infiltration times (ca. 21 h, see Supporting Information), while reptation theory predicts these chains should only partially diffuse into the 100 nm NPG thickness. While further studies are required to fully probe the kinetics of the infiltration process, this data suggests that the kinetics of imbibition is significantly faster than that predicted by polymer reptation and is less strongly dependent on chain $M_w$ than the canonical $\sim N^2$ predicted by the reptation model. A complete study investigating the polymer imbibement kinetics is ongoing and will be presented in future work.

While surface roughness obtained via AFM provides the requisite time for full infiltration *ex situ*, the kinetics of the infiltration can be quantified *in situ* using SE, which is sensitive to changes in optical properties as the pores fill with polymer. Here, the SE model reflects the 3-D microstructure of the NPG, with the pores' refractive index increasing from an initial value of ~1 (air), to a final value of that of either PS (~1.58) or P2VP (~1.56). Figure 3A shows the nanopore fill fraction as a function of infiltration time at 150 °C for PS and P2VP with molecular weights of 64 and 50 kDa, respectively. Figure 3B shows the same data plotted as a function of temperature. We observe that P2VP begins infiltrating into the NPG pores at lower temperatures than PS, presumably due to its lower bulk glass transition temperature (ca. 88 °C for P2VP and ca. 96 °C for PS) and more favorable interaction with NPG. Both PS and P2VP infiltrate slowly in the initial stage and rapidly infiltrate after 0.5 and 5 min, approaching a plateau after 5 and 60 min, respectively. The time for PS to completely infiltrate the NPG is of similar magnitude to those of CaRI experiments with systems of a comparable confinement ratio.[32,47,48] Interestingly, P2VP requires an order of magnitude increase in annealing time to fully infiltrate the NPG film compared to PS. This is despite the two polymers having comparable molecular weights as well as confinement ratios and both being substantially (>50 °C) above their unconfined glass transition temperatures.

A drawback of nanoporous metals is that their structure continually evolves over time, eventually leading to ligament growth and change in porosity.[58,61] This temporal aging is analogous to the thermal coarsening procedure used herein to set the characteristic NPG ligament size. Therefore, one may expect the NPG structure to continuously evolve to form larger-scale ligaments, eventually leading to ligament growth. As such, we investigate the effects of polymer infiltration on temporal aging and optical properties in the PrISM composites. Figure 4 shows bar graphs following the effect of aging on the NPG structure as measured through AFM and SE—the gold ligaments have clearly coalesced into larger


https://doi.org/10.1021/acsami.1c12491
ACS Appl. Mater. Interfaces XXXX, XXX, XXX−XXX

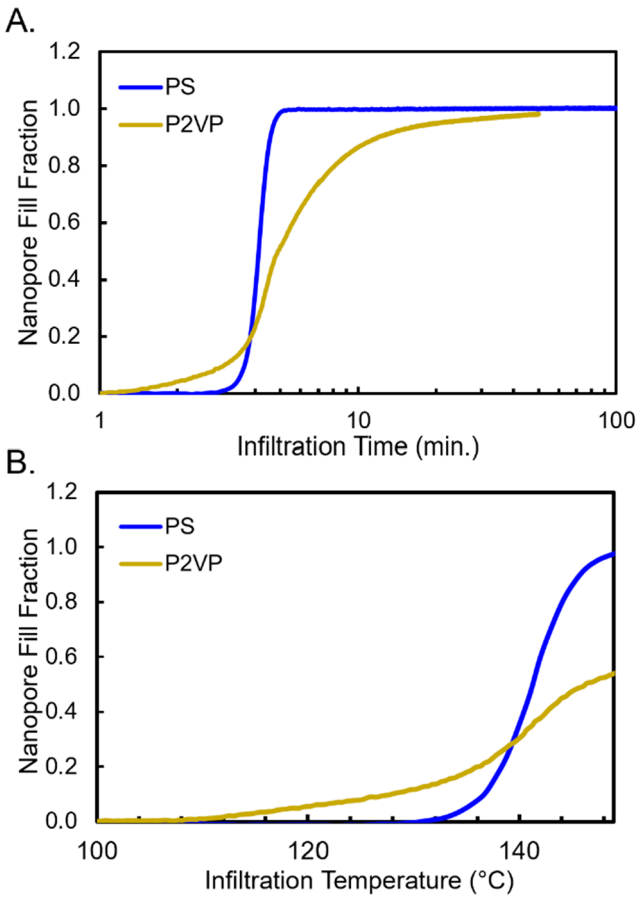


**Figure 3.** Nanopore fill fraction of PS-64 and P2VP-50 as a function of (A) annealing time at 150 °C and (B) annealing temperature as monitored by SE. The fill fraction is defined as $\frac{n(t) - n_{pore}}{n_{poly} - n_{pore}}$, where $n_{pore}$ is the refractive index of the empty pores before infiltration (∼1) and $n_{poly}$ is the refractive index of the infiltrated polymer.

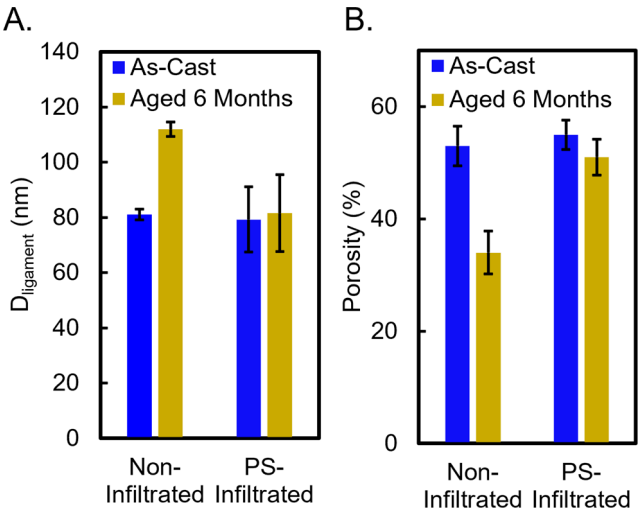


**Figure 4.** Synergistic stabilization of the NPG composites. (A, B) Changes in (A) average ligament size and (B) porosity of the NPG films upon aging for 6 months. The porosity changes are modeled from ellipsometry data; the average ligament sizes are measured from AFM images.

structures after 6 months. To quantify this, AFM analysis indicates the average ligament width, $D_{ligament}$, increases by 30 nm over this time (see Supporting Information). Conversely, the average $D_{ligament}$ of the PS-infiltrated NPG composites does not change (within error) after 6 months, as shown in Figure 4A. Evidently, the infiltrated polymer has substantially hindered coarsening of the NPG film. We attribute this stabilization to the confined polymer that inhibits surface diffusion of the gold atoms, which other work has suggested is the primary cause of thermal coarsening.[56] We also examine the porosity (from SE, see Supporting Information) of noninfiltrated and PS-infiltrated NPG films, both as-cast and aged in Figure 4B. In the case of the PS-infiltrated films, the porosity value is a measure of the relative volume fraction of infiltrated polymer to that of the gold ligaments. The initial porosity of both materials is ca. 53 ± 4%. The porosity of the noninfiltrated NPG drops by approximately 25 ± 3.5% of its original value after 6 months of aging, indicative that temporal aging results in ligament growth. However, there is no such indication in the corresponding data for PS-infiltrated composites.

We note that in addition to the infiltrated polymer substantially hindering the thermal coarsening of the NPG, these PS and P2VP filled PrISM composites lend themselves to mechanical enhancements of the NPG. For support, we look at polymer-infiltrated nanoparticles produced by the CaRI method. The hardness and elastic modulus of these composites increases upon filling the interstitial spaces between nanoparticles with PS. In addition, the high nanofiller fraction (>50 vol %) in CaRI leads to a significant enhancement in nanoscale wear and scratch resistance.[35] In contrast to the films made of discrete particles, the hard phase presented herein forms a bicontinuous morphology with continuous hard (gold) and soft (polymer) phases. It will be interesting to determine whether the infiltration of polymer improves the hardness and elastic modulus observed for CaRI films. However, the viscoelastic properties of the PrISM films should be enhanced by the infiltrated polymer (relative to the pure NPG). This behavior was observed in a nanoporous organosilicate, which is rigid (cohesive fracture energy of 2 J/m$^2$) compared to our flexible polymer−metal hybrid films.[62] In addition to the PrISM composites demonstrating improved nanomechanical properties, the filled metal scaffolds can be used in short-stroke actuator and sensor applications, as demonstrated previously by Detsi et al.,[63] and as flexible all-solid-state submicrometer-thick supercapacitors as demonstrated by Meng and Ding.[64]

**Polymer Glass Transition under Confinement.** We now transition from examining the kinetics of polymer infiltration in NPG to the thermal properties of the resulting composites. Specifically, polymer chains in confined geometries, such as nanosized pores, are expected to have different segmental dynamics than unconfined chains.[36,65−77] The effect of confinement on segmental relaxation dynamics can be captured by measuring the $T_g$ of the polymer using *in situ* SE to monitor changes in the refractive index as a function of temperature. This contrasts with measurements of the infiltration kinetics of the polymer chains (cf. Figure 3), which probes a more global dynamic property that is related to the viscosity of the chains. Figures 5A,B show representative plots of the refractive index versus temperature for a neat ∼130-nm-thick PS-20000 film and the same PS-20000 infiltrated into a NPG film, respectively, demonstrating our ability to measure the polymers' $T_g$ in unconfined and confined systems.


https://doi.org/10.1021/acsami.1c12491
ACS Appl. Mater. Interfaces XXXX, XXX, XXX−XXX

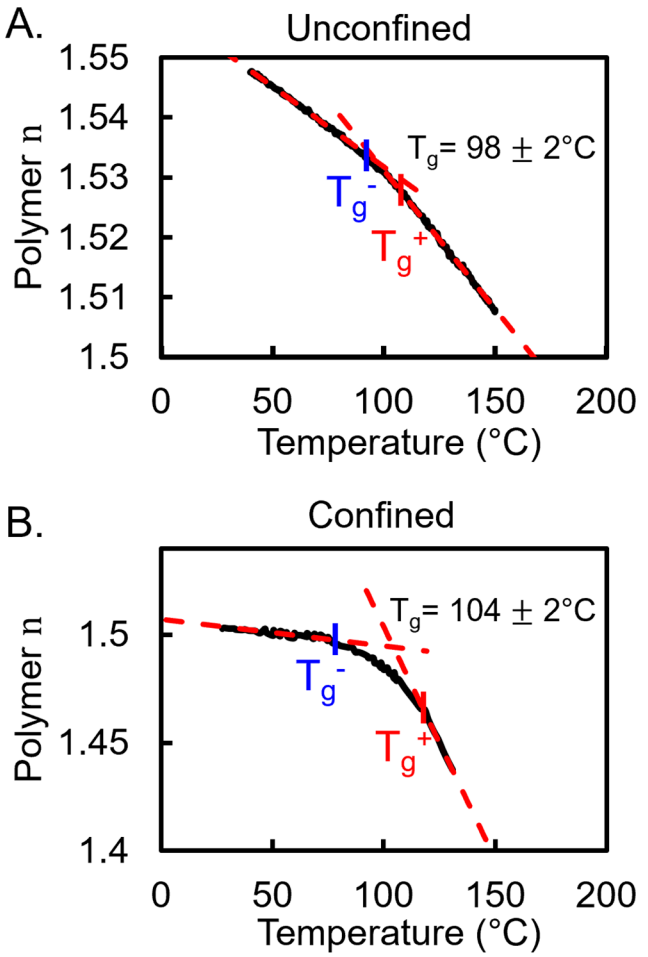


**Figure 5.** Polymer refractive index ($n$) versus temperature for an (A) unconfined 130-nm-thick PS-20000 film and a (B) NPG film infiltrated by the same PS. The $T_g$ of PS increases by ~6 ± 2 °C upon confinement into the pores. Additionally, the $T_g$ breadth, characterized by $T_g^+$ and $T_g^-$, significantly increases.

There are two distinct differences between the data sets. First, the $T_g$ of the confined PS is 6 ± 2 °C higher than the unconfined PS. This difference is attributed to the reduced segmental dynamics of the chain due to confinement within the nanopore with a ~43 nm diameter. Second, the width of the transition for the confined PS is broader than that of the unconfined PS. This difference is quantified by measuring the upper and lower limits of the glass transition temperature, $T_g^+$ and $T_g^-$, respectively, as shown in Figure 5B (see Supporting Information). In Figure 5B, $T_g^-$ appears relatively unchanged compared to the unconfined polymer; however, confinement significantly increases $T_g^+$ from 106 to 119 °C.

Figure 6 shows the change in $T_g$ ($\Delta T_g$), $T_g^+$, and $T_g^-$ for PS and P2VP infiltrated into NPG as a function of the molecular weight. For both polymers, we focus first on $\Delta T_g$, which increases with increasing $M_w$ for both systems. Overall, confined chains of P2VP show a greater increase in $\Delta T_g$ than PS chains of comparable $M_w$. For example, the $\Delta T_g$ of P2VP-850 is 18 ± 2 °C, while this value is only 6 ± 2 °C for PS at a comparable $M_w$. Also, the $\Delta T_g$ of P2VP increases more strongly as a function of $M_w$ compared to that for PS. Both observations point to a greater effective degree of confinement for P2VP chains than for PS chains, despite the pore size being held constant (ca. 43 nm).

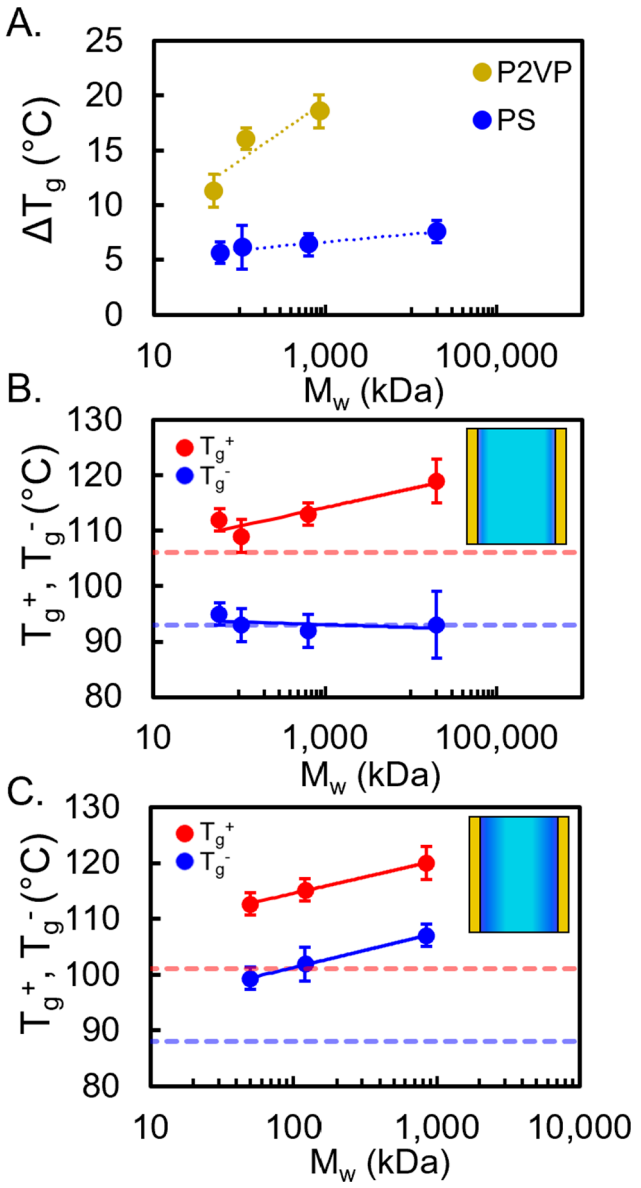


**Figure 6.** (A) $T_g$ increase in confined polymers as a function of the chain $M_w$. Data for both PS and P2VP are shown. (B, C) $T_g^+$ and $T_g^-$ as a function of $M_w$ for (B) PS and (C) P2VP. The light dashed lines in Figure 6B,C show $T_g^+$ and $T_g^-$ of the pure polymers. Inset images are schematics representing the gradient in polymer dynamics confined in the NPG pores.

We now examine how $T_g^+$ and $T_g^-$ depend on polymer type and molecular weight. Figure 6B shows the $T_g^+$ and $T_g^-$ of PS as a function of chain $M_w$ (note: the values for analogous pure PS are shown as dashed lines and do not vary significantly with $M_w$). The $T_g^-$ of PS is relatively constant as $M_w$ increases and does not deviate significantly from values for the unconfined PS. Conversely, $T_g^+$ of PS monotonically increases by up to 10 ± 2 °C as $M_w$ increases from 50 to 20 000 kDa. The greater $\Delta T_g$ at high $M_w$ can be attributed to this increase as well as the increase in the breadth of $T_g$. Recently, it has been shown that the dynamics of adsorbed polymer layers can exhibit a molecular weight dependence, commensurate to what we observe here.[78,79] In polystyrene, this can be related to the slower dynamics at the NPG/PS interface, where chains are potentially strongly adsorbed to the NPG surface. As such,


https://doi.org/10.1021/acsami.1c12491
ACS Appl. Mater. Interfaces XXXX, XXX, XXX−XXX

their dynamics are slowed, increasing the $T_g^+$. The reasonably constant $T_g^-$ value indicates that the dynamics in the regions corresponding to the center of the nanopores behave bulk-like.

In contrast to PS, $T_g^-$ of confined P2VP increases in parallel with the $T_g^+$, resulting in a relatively constant breadth in dynamics, indicating that the polymer dynamics are slowed everywhere as a result of the much stronger interactions of P2VP with the NPG surface compared to the PS.

The microstructure of NPG has been previously studied using SAXS and SEM—however, to our knowledge, there is no prior characterization work conducted using *in situ* SE. Modeling of the ellipsometry data provides an independent measurement of the film porosity and NPG optical properties, which can be compared with typical properties of discrete gold nanorods. Importantly, this allows us to carefully control the gold ligament size through the coarsening temperature and time via *in situ* SE (see Supporting Information). Additionally, we can reliably tune the average NPG pore size, which by extension, allows for precise control over the degree of geometric confinement in these composites. These nanoporous metal films are thus a versatile architecture that can be systematically varied to produce a wide array of conditions from a single starting material. This is a unique benefit over other classes of polymer nanocomposites, which are similarly broadly tunable but often require the synthesis of new materials or multistep processes. Additionally, by changing the composition of the precursor alloy, the ability to vary the relative ratio of organic to inorganic constituents is achievable—for example, NPG scaffolds fabricated from a 6-karat leaf ($Au_{25}Ag_{75}$ alloy) have a porosity of ~66 ± 5% as measured using SE as opposed to the 12-karat leaf used here with 53 ± 4% porosity (see Supporting Information). Importantly, the precursor metal films can be fabricated from a variety of metals,[80−82] further expanding on the available parameter space for these materials such as polymer wettability.

We now turn to understanding the synergistic PrISM composites and their resultant properties. The differing polymer infiltration times of PS and P2VP can be understood by considering the relative interactions of PS and P2VP with the NPG. Past work on polymers under confinement[41,83−85] has shown that the mechanism of polymer infiltration is fundamentally affected by the interaction strength between the polymer and inorganic filler material. For strongly interacting systems, infiltration is adhesion-dominated, where chains adsorb to the confinement surface and move more slowly through the void spaces compared to weakly interacting systems, where infiltration is diffusion-dominated. More specifically, for strongly adsorbed polymer chains, a "dead zone" is created, thus reducing the pore radius and leading to an increase in the imbibing polymer's effective viscosity.[84] This is due to the formation of polymer loops along the confining wall, which increase the number of topological constraints for other imbibing chains. These imbibing chains can entangle with the loops of the adsorbed chains and thus increase the size of the "dead zone".[83] Gold and P2VP have strongly favorable interactions,[18] which is observed here as decreased infiltration kinetics of P2VP infiltration. Specifically, as demonstrated in Figure 3, P2VP begins infiltrating much sooner (and faster) than PS but then significantly slows down with time. This can be interpreted as the buildup of the "dead zone" in P2VP due to its much stronger attraction to gold (i.e., fast initial infiltration due to no "dead zone" but then slows down with time due to the adsorbed P2VP chains and much greater confinement). This idea is further supported by the slower segmental dynamics near the pore wall for P2VP compared to PS and an overall greater increase in $T_g$. This observation suggests that wettability (e.g., surface interactions) dominates the infiltration behavior as opposed to other factors such as chain molecular weight. These results are consistent with adhesion-limited infiltration.

While the strength of interactions between NPG/PS is relatively weaker compared to NPG/P2VP, the interactions are still strong enough, that combined with the expansive surface area of the gold ligament structure, the result is slower segmental relaxation at those interfaces. This is observed as increased $T_g^+$, resulting in the slight increase in $T_g$ seen in the PS-based composites. However, since the interaction strength between gold and PS is comparatively weak, the dynamics at the center of the pores remain bulk-like, as observed by the similar value of $T_g^-$ with that of the bulk, indicating that fewer adsorption sites are present, making the PS infiltration dynamics relatively faster than P2VP. This is shown schematically in the inset of Figure 6B where dark blue represents confined polymer chains and light blue represents unconfined chains. Conversely, the increased interaction strength between gold and P2VP slows down the relaxation dynamics throughout the entire NPG pore (Figure 6C, inset). The result is a greater increase in the overall polymer $T_g$ but without any significant change to the breadth of the $T_g$.

In this study, the pore diameter is fixed at ~43 nm. As noted previously, the pore size can be tuned from 10−100s of nm. We therefore expect that polymer chain dynamics can be further manipulated depending on the imposed degree of confinement. For the case of $L_{pore}/2R_g \gg 1$, the chains are unconfined and should exhibit bulk-like behavior, with little-to-no change in $T_g$. When the pore size is decreased such that it is comparable in size to that of the polymers, the segmental dynamics of the polymers decrease, resulting in an increase in $T_g$ as demonstrated herein. However, when reducing the pore size to the lower limit of the nanometer range (i.e., $L_{pore}/2R_g \ll 1$), interesting phenomena are expected to occur; Doi et al.[84] recently showed that strong chain confinement leads to chain disentanglement, leading to faster infiltration kinetics. Experiments are currently underway to quantify the change in $T_g$ across this broad range of pore sizes. Overall, these bicontinuous materials appear to have a synergistic stabilization effect—the addition of the polymer stabilizes the gold ligaments from coarsening, while the geometrical confinement of the polymer within the NPG reduces the segmental dynamics of the polymer chains, increasing their $T_g$.

## CONCLUSIONS

We have fabricated a new class of polymer nanocomposites utilizing intrinsically percolated NPG infiltrated with polymer chains to form bicontinuous organic−inorganic materials. The average pore size of the underlying nanoporous film can be systematically tuned through coarsening via thermal treatment, allowing scaffolds with varying levels of polymer confinement to be produced from a single material. Polymer chains are readily infiltrated into the porous network through heating above the polymer $T_g$, and the relative kinetics of the infiltration process is related to the interaction strengths between the metal scaffold and polymer. The bicontinuous components cooperatively stabilize each other, where small pore sizes serve to reduce polymer segmental dynamics and the


https://doi.org/10.1021/acsami.1c12491
ACS Appl. Mater. Interfaces XXXX, XXX, XXX−XXX

presence of the polymer restricts coarsening and ligament growth of the NPG scaffold. These materials represent a new pathway for designing hybrid composites with enhanced properties—including ionic conductivity and mechanical response—that are a result of the intrinsically percolated mesoporous structure. The ability to manipulate the relative confinement of the polymer chains as well as the polymer–scaffold interactions provides an expansive test bed to probe the underlying polymer physics in these geometries.

## MATERIALS AND METHODS

**Materials.** Nanoporous gold (NPG) films were prepared by free corrosion dealloying of ∼100-nm-thick Au–Ag alloy leaves with a composition of $Au_{35}Ag_{65}$ (at %) in 15.8 M nitric acid (NORIS Blattgoldfabrik) for approximately 30 min using a previously developed procedure that selectively etches the silver.[49,61,86] Polystyrene (PS) and poly(2-vinylpyridine) (P2VP) were purchased from Polymer Source Inc. and used as received. The weight-average molecular weights, polydispersity index, and estimated radius of gyration measured from DLS for all samples are summarized in Table 1. N-type, <100> oriented silicon wafers (dopant Ph, 10–20 Ω·cm resistivity, 475–575 μm thickness, single side polished) were purchased from Silicon Quest International and washed with methanol and toluene and dried under nitrogen flow.

**Methods.** *NPG/Polymer Composite Preparation.* PS and P2VP polymers with varying molecular weights were dissolved in toluene (99.9%, for HPLC, Sigma-Aldrich) and *n*-butanol (≥99.9%, Sigma-Aldrich), respectively, and stirred for 24 h using a rotating magnetic stir bar. The solutions (2.4 wt %) were spin-coated (4000 rpm, 60 s, Laurell Technologies) onto 1 × 1 $cm^2$ cleaned silicon wafers and dried at 100 °C for 1 h to remove residual solvent. All films were smooth and homogeneous as-cast. Film thicknesses were measured with a white-light reflectometer (Filmetrics F3–UV) and ranged from 90–130 nm depending on the polymer molecular weight. NPG films were coarsened to a desirable pore size through thermal treatment on a hot stage (Mettler FP-82, Mettler Toledo, INC.) under continuous argon flow at 175 °C for 3 h and immediately quenched to ambient conditions. The coarsened NPG films were then floated on DI $H_2O$. After it was lifted from its substrate, the NPG was stacked on top of the PS and P2VP polymer films and dried on a hot plate at 60 °C for 30 min to remove residual DI $H_2O$. Macroscopic wrinkling of the NPG film was not apparent during this bilayer preparation. The bilayer films were then annealed on the same hot stage for 3 h at a set temperature of 150 °C to induce polymer infiltration. This temperature was specifically chosen to impart polymer mobility while also preventing further NPG coarsening.

*Atomic Force Microscopy (AFM).* Tapping mode AFM was performed using an Agilent 5420 AFM with noncontact tips (TAP300AL-G-50 radius of curvature <10 nm, Ted Pella). The images were processed using Gwyddion software. Gold ligament and nanopore dimensions were computed by individually measuring at least 500 features across five separate 2 × 2 $\mu m^2$ images. Radial autocorrelation function analysis was performed to determine the characteristic NPG ligament dimension.

*Scanning Electron Microscopy (SEM).* Stacked NPG/polymer bilayers and infiltrated composite samples were submerged in liquid nitrogen for several minutes to decrease the ductility of the NPG. The samples were then scored with a diamond scribe and fractured. Cross-sectional backscattered electron micrographs were taken with an FEI Quanta 600 environmental scanning electron microscope (ESEM) at 15 keV.

*Dynamic Light Scattering (DLS).* DLS was performed using a Malvern Zetasizer nano-s DLS with a 632.8 nm red laser to determine the hydrodynamic radii ($R_h$) of PS and P2VP as a function of molecular weight. The two polymers were dissolved in toluene and *n*-butanol, respectively, at a dilute concentration of 0.05 mg/mL. The $R_h$ values for each polymer are then extracted by plotting the number distribution vs species diameter and fitting the data with a Gaussian function.

*Small-Angle X-ray Scattering (SAXS).* SAXS was used to determine the center-to-center ligament distance of the NPG films before and after coarsening. To prepare NPG films for SAXS characterization, the NPG films were floated on DI $H_2O$. After it was lifted from its substrate, the NPG was transferred to a Kapton film and dried on a hot plate at 60 °C for 30 min to remove residual DI $H_2O$. SAXS measurements were performed on a Xenocs Xeuss 2.0 at the University of Pennsylvania, with a sample-to-detector distance of 6.36 m with a Cu K$\alpha$ source, providing an available *q*-range of 0.003–0.09 $Å^{-1}$. Raw 2-D scattering spectra were collected on a Pilatus 1 M detector for 20 min per sample and were then azimuthally integrated into 1-D patterns for analysis.

*Spectroscopic Ellipsometry (SE).* The optical properties of unfilled NPG and infiltrated composite materials were probed using spectroscopic ellipsometry (M2000, J.A. Woollam, NE) with a spectral range of 400–1600 nm and equipped with a thermocontrolled stage (Linkam Corp., U.K.). All SE samples were prepared using frosted glass substrates in place of silicon to minimize backscattering. Measurements of the unfilled NPG optical properties were conducted at five different incident light angles with an acquisition time of 10 s per angle. The measured optical response was modeled using a harmonic oscillator model in the wavelength range of 450–1050 nm. The harmonic oscillator model was used in subsequent experiments that probed the *in situ* optical response of the NPG pores. More information on the modeling procedure is provided in the Supporting Information.

*In situ* polymer infiltration experiments were performed by heating stacked bilayers of NPG and polymer to 150 °C at a ramp of 25 °C/min at a single angle of incident light (70°) for predetermined amounts of time; the acquisition time of each measurement was 1 s. The samples were subsequently cooled to room temperature. Glass transition temperature measurements were performed by heating the infiltrated NPG composites to 150 °C for 10 min and then cooling to 25 °C at a constant cooling rate of 10 °C/min.

## ASSOCIATED CONTENT

### Supporting Information

The Supporting Information is available free of charge at https://pubs.acs.org/doi/10.1021/acsami.1c12491.

Expanded discussion of AFM imaging and analysis, spectroscopic ellipsometry data modeling procedure and example, additional SAXS data, TEM images, and SEM images of NPG films and NPG/polymer composites (PDF)

## AUTHOR INFORMATION


### Corresponding Authors

**Russell J. Composto** – *Department of Materials Science and Engineering, University of Pennsylvania, Philadelphia, Pennsylvania 19104, United States;* orcid.org/0000-0002-5906-2594; Email: composto@seas.upenn.edu

**Zahra Fakhraai** – *Department of Chemistry, University of Pennsylvania, Philadelphia, Pennsylvania 19104, United States;* orcid.org/0000-0002-0597-9882; Email: fakhraai@sas.upenn.edu

### Authors

**Shawn M. Maguire** – *Department of Materials Science and Engineering, University of Pennsylvania, Philadelphia, Pennsylvania 19104, United States;* orcid.org/0000-0002-5317-4990

**Connor R. Bilchak** – *Department of Materials Science and Engineering and Department of Chemistry, University of*




https://doi.org/10.1021/acsami.1c12491
ACS Appl. Mater. Interfaces XXXX, XXX, XXX–XXX

*Pennsylvania, Philadelphia, Pennsylvania 19104, United States;* orcid.org/0000-0001-8815-1601

**John S. Corsi** − *Department of Materials Science and Engineering, University of Pennsylvania, Philadelphia, Pennsylvania 19104, United States*

**Samuel S. Welborn** − *Department of Materials Science and Engineering, University of Pennsylvania, Philadelphia, Pennsylvania 19104, United States*

**Theresa Tsaggaris** − *Department of Materials Science and Engineering, University of Pennsylvania, Philadelphia, Pennsylvania 19104, United States*

**Jamie Ford** − *Nanoscale Characterization Facility, Singh Center for Nanotechnology, University of Pennsylvania, Philadelphia, Pennsylvania 19104, United States*

**Eric Detsi** − *Department of Materials Science and Engineering, University of Pennsylvania, Philadelphia, Pennsylvania 19104, United States;* orcid.org/0000-0002-4009-7260

Complete contact information is available at: https://pubs.acs.org/10.1021/acsami.1c12491

### Author Contributions

Z.F. and R.J.C. designed and supervised this work. S.M.M., C.R.B., J.S.C., S.S.W., T.T., and J.F. carried out experiments. S.M.M. and C.R.B. analyzed experimental results. S.M.M., C.R.B., and S.S.W. prepared schematics. The manuscript was written and edited through contributions of all authors. All authors have given approval to the final version of the manuscript.

### Author Contributions

[‖]S.M.M. and C.R.B. contributed equally.

### Notes

The authors declare no competing financial interest.

## ■ ACKNOWLEDGMENTS

S.M.M. and C.R.B were supported by the National Science Foundation Partnerships for International Research and Education program (NSF-PIRE) Grant #1545884. T.T. was supported by the National Science Foundation Louis Stokes Alliance for Minority Participation (LSAMP). R.J.C. and Z.F. were partially supported by NSF MRSEC DMR-1720530. R.J.C. and S.M.M. were also partially funded by the NSF grant DMR-1905912. J.S.C. acknowledges financial support from the Vagelos Institute for Energy Science and Technology (VIEST) through the 2018 VIEST Fellowship. The authors acknowledge use of the Dual Source and Environmental X-ray Scattering facility operated by the Laboratory for Research on the Structure of Matter at the University of Pennsylvania (NSF MRSEC DMR-1720530). The equipment purchase was made possible by an NSF MRI grant (17-25969), an ARO DURIP grant (W911NF17-1-0282), and the University of Pennsylvania. Additionally, this work was carried out in part at the Singh Center for Nanotechnology, which is supported by the NSF National Nanotechnology Coordinated Infrastructure Program under grant NNCI-2025608. The authors gratefully acknowledge the use of facilities and instrumentation (DLS) supported by the Materials Science and Engineering Departmental Laboratory at the University of Pennsylvania. The authors also acknowledge Dr. Daeyeon Lee and Dr. Robert A. Riggleman for helpful discussions.

## ■ REFERENCES

(1) Guth, E. Theory of Filler Reinforcement. *J. Appl. Phys.* **1945**, *16* (1), 20−25.

(2) Balazs, A. C.; Emrick, T.; Russell, T. P. Nanoparticle Polymer Composites: Where Two Small Worlds Meet. *Science (Washington, DC, U. S.)* **2006**, *314* (5802), 1107−1110.

(3) Bilchak, C. R.; Buenning, E.; Asai, M.; Zhang, K.; Durning, C. J.; Kumar, S. K.; Huang, Y.; Benicewicz, B. C.; Gidley, D. W.; Cheng, S.; Sokolov, A. P.; Minelli, M.; Doghieri, F. Polymer-Grafted Nanoparticle Membranes with Controllable Free Volume. *Macromolecules* **2017**, *50* (18), 7111−7120.

(4) Merkel, T. C.; Freeman, B. D.; Spontak, R. J.; He, Z.; Pinnau, I.; Meakin, P.; Hill, a J. Ultrapermeable, Reverse-Selective Nanocomposite Membranes. *Science* **2002**, *296* (5567), 519−522.

(5) Glor, E. C.; Ferrier, R. C.; Li, C.; Composto, R. J.; Fakhraai, Z. Out-of-Plane Orientation Alignment and Reorientation Dynamics of Gold Nanorods in Polymer Nanocomposite Films. *Soft Matter* **2017**, *13* (11), 2207−2215.

(6) Hore, M. J. A.; Frischknecht, A. L.; Composto, R. J. Nanorod Assemblies in Polymer Films and Their Dispersion - Dependent Optical Properties. *ACS Macro Lett.* **2012**, *1* (1), 115−121.

(7) Hore, M. J. A.; Composto, R. J. Nanorod Self-Assembly for Tuning Optical Absorption. *ACS Nano* **2010**, *4* (11), 6941−6949.

(8) Bilchak, C. R.; Huang, Y.; Benicewicz, B. C.; Durning, C. J.; Kumar, S. K. High-Frequency Mechanical Behavior of Pure Polymer-Grafted Nanoparticle Constructs. *ACS Macro Lett.* **2019**, *8* (3), 294−298.

(9) Rittigstein, P.; Torkelson, J. M. Polymer-Nanoparticle Interfacial Interactions in Polymer Nanocomposites: Confinement Effects on Glass Transition Temperature and Suppression of Physical Aging. *J. Polym. Sci., Part B: Polym. Phys.* **2006**, *44*, 2935.

(10) Polizos, G.; Tuncer, E.; Agapov, A. L.; Stevens, D.; Sokolov, A. P.; Kidder, M. K.; Jacobs, J. D.; Koerner, H.; Vaia, R. A.; More, K. L.; Sauers, I. Effect of Polymer-Nanoparticle Interactions on the Glass Transition Dynamics and the Conductivity Mechanism in Polyurethane Titanium Dioxide Nanocomposites. *Polymer* **2012**, *53* (2), 595−603.

(11) Takahashi, S.; Paul, D. R. Gas Permeation in Poly(Ether Imide) Nanocomposite Membranes Based on Surface-Treated Silica. Part 1: Without Chemical Coupling to Matrix. *Polymer* **2006**, *47* (21), 7519−7534.

(12) Chevigny, C.; Dalmas, F.; Di Cola, E.; Gigmes, D.; Bertin, D.; Boué, F.; Jestin, J. Polymer-Grafted-Nanoparticles Nanocomposites: Dispersion, Grafted Chain Conformation, and Rheological Behavior. *Macromolecules* **2011**, *44* (1), 122−133.

(13) Natarajan, B.; Li, Y.; Deng, H.; Brinson, L. C.; Schadler, L. S. Effect of Interfacial Energetics on Dispersion and Glass Transition Temperature in Polymer Nanocomposites. *Macromolecules* **2013**, *46* (7), 2833−2841.

(14) Wagner, H. D.; Vaia, R. A. Nanocomposites: Issues at the Interface. *Mater. Today* **2004**, *7* (11), 38−42.

(15) Schadler, L. S.; Brinson, L. C.; Sawyer, W. G. Polymer Nanocomposites: A Small Part of the Story. *JOM* **2007**, *59* (3), 53−60.

(16) Maguire, S. M.; Chung, H. J.; Composto, R. J. CHAPTER 4: Polymer Blend Systems with an Added Solvent. *Bijels* **2020**, 73.

(17) Chung, H. J.; Ohno, K.; Fukuda, T.; Composto, R. J. Self-Regulated Structures in Nanocomposites by Directed Nanoparticle Assembly. *Nano Lett.* **2005**, *5* (10), 1878−1882.

(18) Kim, B. J.; Bang, J.; Hawker, C. J.; Kramer, E. J. Effect of Areal Chain Density on the Location of Polymer-Modified Gold Nanoparticles in a Block Copolymer Template. *Macromolecules* **2006**, *39* (12), 4108−4114.

(19) Chen, Q.; Gong, S.; Moll, J.; Zhao, D.; Kumar, S. K.; Colby, R. H. Mechanical Reinforcement of Polymer Nanocomposites from Percolation of a Nanoparticle Network. *ACS Macro Lett.* **2015**, *4* (4), 398−402.

(20) Moll, J. F.; Akcora, P.; Rungta, A.; Gong, S.; Colby, R. H.; Benicewicz, B. C.; Kumar, S. K. Mechanical Reinforcement in

Polymer Melts Filled with Polymer Grafted Nanoparticles. *Macromolecules* **2011**, *44* (18), 7473−7477.
(21) Zhao, D.; Ge, S.; Senses, E.; Akcora, P.; Jestin, J.; Kumar, S. K. Role of Filler Shape and Connectivity on the Viscoelastic Behavior in Polymer Nanocomposites. *Macromolecules* **2015**, *48* (15), 5433−5438.
(22) Favier, V.; Chanzy, H.; Cavaillé, J. Y. Polymer Nanocomposites Reinforced by Cellulose Whiskers. *Macromolecules* **1995**, *28* (18), 6365−6367.
(23) Wang, Y.; Cao, X.; Zhang, L. Effects of Cellulose Whiskers on Properties of Soy Protein Thermoplastics. *Macromol. Biosci.* **2006**, *6* (7), 524−531.
(24) Favier, V.; Canova, G. R.; Shrivastava, S. C.; Cavaillé, J. Y. Mechanical Percolation in Cellulose Whisker Nanocomposites. *Polym. Eng. Sci.* **1997**, *37* (10), 1732−1739.
(25) Du, F.; Scogna, R. C.; Zhou, W.; Brand, S.; Fischer, J. E.; Winey, K. I. Nanotube Networks in Polymer Nanocomposites: Rheology and Electrical Conductivity. *Macromolecules* **2004**, *37* (24), 9048−9055.
(26) Du, F.; Fischer, J. E.; Winey, K. I. Effect of Nanotube Alignment on Percolation Conductivity in Carbon Nanotube/Polymer Composites. *Phys. Rev. B: Condens. Matter Mater. Phys.* **2005**, *72* (12), 1−4.
(27) Bonnet, P.; Sireude, D.; Garnier, B.; Chauvet, O. Thermal Properties and Percolation in Carbon Nanotube-Polymer Composites. *Appl. Phys. Lett.* **2007**, *91* (20), 201910.
(28) Maréchal, M.; Niepceron, F.; Gebel, G.; Mendil-Jakani, H.; Galiano, H. Inside the Structure of a Nanocomposite Electrolyte Membrane: How Hybrid Particles Get along with the Polymer Matrix. *Nanoscale* **2015**, *7* (7), 3077−3087.
(29) Shen, Y.; Lin, Y.; Li, M.; Nan, C. W. High Dielectric Performance of Polymer Composite Films Induced by a Percolating Interparticle Barrier Layer. *Adv. Mater.* **2007**, *19* (10), 1418−1422.
(30) Li, C.; Han, J.; Ryu, C. Y.; Benicewicz, B. C. A Versatile Method To Prepare RAFT Agent Anchored Substrates and the Preparation of PMMA Grafted Nanoparticles. *Macromolecules* **2006**, *39* (9), 3175−3183.
(31) Cong, H.; Hu, X.; Radosz, M.; Shen, Y. Brominated Poly (2, 6-Diphenyl-1, 4-Phenylene Oxide) and Its Silica Nanocomposite Membranes for Gas Separation. *Ind. Eng. Chem. Res.* **2007**, *46*, 2567−2575.
(32) Novak, B. M. Hybrid Nanocomposite Materials—between Inorganic Glasses and Organic Polymers. *Adv. Mater.* **1993**, *5* (6), 422−433.
(33) Jouault, N.; Vallat, P.; Dalmas, F.; Said, S.; Jestin, J.; Boue, F. Well-Dispersed Fractal Aggregates as Filler in Polymer-Silica Nanocomposites: Long-Range Effects in Rheology. *Macromolecules* **2009**, *42* (6), 2031−2040.
(34) Hashimoto, M.; Takadama, H.; Mizuno, M.; Kokubo, T. Mechanical Properties and Apatite Forming Ability of TiO2 Nanoparticles/High Density Polyethylene Composite: Effect of Filler Content. *J. Mater. Sci.: Mater. Med.* **2007**, *18* (4), 661−668.
(35) Huang, Y.; Jiang, Y.; Hor, J. L.; Gupta, R.; Zhang, L.; Stebe, K. J.; Feng, G.; Turner, K. T.; Lee, D. Polymer Nanocomposite Films with Extremely High Nanoparticle Loadings via Capillary Rise Infiltration (CaRI). *Nanoscale* **2015**, *7*, 798−805.
(36) Wang, H.; Hor, J. L.; Zhang, Y.; Liu, T.; Lee, D.; Fakhraai, Z. Dramatic Increase in Polymer Glass Transition Temperature under Extreme Nanoconfinement in Weakly Interacting Nanoparticle Films. *ACS Nano* **2018**, *12*, 5580−5587.
(37) Akcora, P.; Liu, H.; Kumar, S. K.; Moll, J.; Li, Y.; Benicewicz, B. C.; Schadler, L. S.; Acehan, D.; Panagiotopoulos, A. Z.; Pryamitsyn, V.; Ganesan, V.; Ilavsky, J.; Thiyagarajan, P.; Colby, R. H.; Douglas, J. F. Anisotropic Self-Assembly of Spherical Polymer-Grafted Nanoparticles. *Nat. Mater.* **2009**, *8*, 354.
(38) Yan, H.; Tang, Y.; Long, W.; Li, Y. Enhanced Thermal Conductivity in Polymer Composites with Aligned Graphene Nanosheets. *J. Mater. Sci.* **2014**, *49* (15), 5256−5264.
(39) Ralphs, M.; Kong, W.; Wang, R. Y.; Rykaczewski, K. Thermal Conductivity Enhancement of Soft Polymer Composites through Magnetically Induced Percolation and Particle−Particle Contact Engineering. *Adv. Mater. Interfaces* **2019**, *6* (6), 1801857.
(40) Detsi, E.; Vuković, Z.; Punzhin, S.; Bronsveld, P. M.; Onck, P. R.; Hosson, J. T. M. D. Fine-Tuning the Feature Size of Nanoporous Silver. *CrystEngComm* **2012**, *14* (17), 5402−5406.
(41) Venkatesh, R. B.; Zhang, T.; Manohar, N.; Stebe, K. J.; Riggleman, R. A.; Lee, D. Effect of Polymer−Nanoparticle Interactions on Solvent-Driven Infiltration of Polymer (SIP) into Nanoparticle Packings: A Molecular Dynamics Study. *Mol. Syst. Des. Eng.* **2020**, *5* (3), 666.
(42) Detsi, E.; Van De Schootbrugge, M.; Punzhin, S.; Onck, P. R.; De Hosson, J. T. M. On Tuning the Morphology of Nanoporous Gold. *Scr. Mater.* **2011**, *64* (4), 319−322.
(43) Detsi, E.; Sellès, M. S.; Onck, P. R.; De Hosson, J. T. M. Nanoporous Silver as Electrochemical Actuator. *Scr. Mater.* **2013**, *69*, 195−198.
(44) Wang, L.; Welborn, S. S.; Kumar, H.; Li, M.; Wang, Z.; Shenoy, V. B.; Detsi, E. High-Rate and Long Cycle-Life Alloy-Type Magnesium-Ion Battery Anode Enabled Through (De)-Magnesiation-Induced Near-Room-Temperature Solid−Liquid Phase Transformation. *Adv. Energy Mater.* **2019**, *9* (45), 1902086.
(45) Wang, K.; Kobler, A.; Kübel, C.; Jelitto, H.; Schneider, G.; Weissmüller, J. Nanoporous-Gold-Based Composites: Toward Tensile Ductility. *NPG Asia Mater.* **2015**, *7* (6), e187.
(46) Wang, K.; Weissmüller, J. Composites of Nanoporous Gold and Polymer. *Adv. Mater.* **2013**, *25* (9), 1280−1284.
(47) Gnegel, S.; Li, J.; Mameka, N.; Huber, N.; Düster, A. Numerical Investigation of Polymer Coated Nanoporous Gold. *Materials* **2019**, *12* (13), 2178.
(48) Mameka, N.; Wang, K.; Markmann, J.; Lilleodden, E. T.; Weissmüller, J. Nanoporous Gold—Testing Macro-Scale Samples to Probe Small-Scale Mechanical Behavior. *Mater. Res. Lett.* **2016**, *4* (1), 27−36.
(49) Detsi, E.; Onck, P.; De Hosson, J. T. M. Metallic Muscles at Work: High Rate Actuation in Nanoporous Gold/Polyaniline Composites. *ACS Nano* **2013**, *7* (5), 4299−4306.
(50) Li, Y.; Liu, Y.; Liu, J.; Liu, J.; Tang, H.; Cao, C.; Zhao, D.; Ding, Y. Molecularly Imprinted Polymer Decorated Nanoporous Gold for Highly Selective and Sensitive Electrochemical Sensors. *Sci. Rep.* **2015**, *5*, 33−35.
(51) Roschning, B.; Weissmüller, J. Nanoporous-Gold-Polypyrrole Hybrid Materials for Millimeter-Sized Free Standing Actuators. *Adv. Mater. Interfaces* **2020**, *7* (24), 2001415.
(52) Kim, B. J.; Fredrickson, G. H.; Kramer, E. J. Effect of Polymer Ligand Molecular Weight on Polymer-Coated Nanoparticle Location in Block Copolymers. *Macromolecules* **2008**, *41* (2), 436−447.
(53) Liu, Z.; Chang, T.; Huang, H.; He, T. Gold Nanoparticle Arrays Assembled on the Reconstructed Surface of Block Copolymer Thin Films. *RSC Adv.* **2013**, *3* (43), 20464−20470.
(54) Lee, J.; Kwak, J.; Choi, C.; Han, S. H.; Kim, J. K. Phase Behavior of Poly(2-Vinylpyridine)-Block-Poly(4-Vinylpyridine) Copolymers Containing Gold Nanoparticles. *Macromolecules* **2017**, *50* (23), 9373−9379.
(55) Welborn, S. S.; Detsi, E. Small-Angle X-Ray Scattering of Nanoporous Materials. *Nanoscale Horizons* **2020**, *5* (1), 12−24.
(56) Viswanath, R. N.; Chirayath, V. A.; Rajaraman, R.; Amarendra, G.; Sundar, C. S. Ligament Coarsening in Nanoporous Gold: Insights from Positron Annihilation Study. *Appl. Phys. Lett.* **2013**, *102* (25), 253101.
(57) Welborn, S. S.; Van Der Meer, S.; Corsi, J. S.; De Hosson, J. T. M.; Detsi, E. Using X-Ray Scattering to Elucidate the Microstructural Instability of 3D Bicontinuous Nanoporous Metal Scaffolds for Use in an Aperiodic 3D Tricontinuous Conductor-Insulator-Conductor Nanocapacitor. *ACS Appl. Mater. Interfaces* **2021**, *13*, 11721.
(58) Chen-Wiegart, Y. C. K.; Wang, S.; Chu, Y. S.; Liu, W.; McNulty, I.; Voorhees, P. W.; Dunand, D. C. Structural Evolution of


https://doi.org/10.1021/acsami.1c12491
ACS Appl. Mater. Interfaces XXXX, XXX, XXX−XXX

Nanoporous Gold during Thermal Coarsening. *Acta Mater.* **2012**, *60* (12), 4972−4981.
(59) Huang, Y.; Jiang, Y.; Hor, J. L.; Gupta, R.; Zhang, L.; Stebe, K. J.; Feng, G.; Turner, K. T.; Lee, D. Polymer Nanocomposite Films with Extremely High Nanoparticle Loadings via Capillary Rise Infilitration (CaRI). *Nanoscale* **2015**, *7*, 798−805.
(60) Green, P. F.; Kramer, E. J. Temperature Dependence of Tracer Diffusion Coefficients in Polystyrene. *J. Mater. Res.* **1986**, *1* (1), 202−204.
(61) Erlebacher, J.; Aziz, M. J.; Karma, A.; Dimitrov, N.; Sieradzki, K. Evolution of Nanoporosity in Dealloying. *Nature* **2001**, *410* (6827), 450−453.
(62) Isaacson, S. G.; Lionti, K.; Volksen, W.; Magbitang, T. P.; Matsuda, Y.; Dauskardt, R. H.; Dubois, G. Fundamental Limits of Material Toughening in Molecularly Confined Polymers. *Nat. Mater.* **2016**, *15* (3), 294−298.
(63) Detsi, E.; Chen, Z. G.; Vellinga, W. P.; Onck, P. R.; De Hosson, J. T. M. Actuating and Sensing Properties of Nanoporous Gold. *J. Nanosci. Nanotechnol.* **2012**, *12* (6), 4951−4955.
(64) Meng, F.; Ding, Y. Sub-Micrometer-Thick All-Solid-State Supercapacitors with High Power and Energy Densities. *Adv. Mater.* **2011**, *23* (35), 4098−4102.
(65) Hor, J. L.; Wang, H.; Fakhraai, Z.; Lee, D. Effect of Physical Nanoconfinement on the Viscosity of Unentangled Polymers during Capillary Rise Infilitration. *Macromolecules* **2018**, *51*, 5069.
(66) Koh, Y. P.; Li, Q.; Simon, S. L. Tg and Reactivity at the Nanoscale. *Thermochim. Acta* **2009**, *492*, 45−50.
(67) Zheng, W.; Simon, S. L. Confinement Effects on the Glass Transition of Hydrogen Bonded Liquids. *J. Chem. Phys.* **2007**, *127* (19), 194501.
(68) Jackson, C. L.; McKenna, G. B. The Glass Transition of Organic Liquids Confined to Small Pores. *J. Non-Cryst. Solids* **1991**, *131*−*133*, 221−224.
(69) Chen, J.; Li, L.; Zhou, D.; Wang, X.; Xue, G. Effect of Geometric Curvature on Vitrification Behavior for Polymer Nanotubes Confined in Anodic Aluminum Oxide Templates. *Phys. Rev. E - Stat. Nonlinear, Soft Matter Phys.* **2015**, *92* (3), 1−8.
(70) Fakhraai, Z.; Lee, D.; Hor, J. L.; Wang, H. Effects of Polymer−Nanoparticle Interactions on the Viscosity of Unentangled Polymers under Extreme Nanoconfinement during Capillary Rise Infiltration. *Soft Matter* **2018**, *14* (13), 2438.
(71) Alexandris, S.; Papadopoulos, P.; Sakellariou, G.; Steinhart, M.; Butt, H. J.; Floudas, G. Interfacial Energy and Glass Temperature of Polymers Confined to Nanoporous Alumina. *Macromolecules* **2016**, *49* (19), 7400−7414.
(72) Li, L.; Zhou, D.; Huang, D.; Xue, G. Double Glass Transition Temperatures of Poly(Methyl Methacrylate) Confined in Alumina Nanotube Templates. *Macromolecules* **2014**, *47* (1), 297−303.
(73) Wang, H.; Kearns, K. L.; Zhang, A.; Arabi Shamsabadi, A.; Jin, Y.; Bond, A.; Hurney, S. M.; Morillo, C.; Fakhraai, Z. Effect of Nanopore Geometry in the Conformation and Vibrational Dynamics of a Highly Confined Molecular Glass. *Nano Lett.* **2021**, *21* (4), 1778−1784.
(74) Zhang, C.; Guo, Y.; Priestley, R. D. Glass Transition Temperature of Polymer Nanoparticles under Soft and Hard Confinement. *Macromolecules* **2011**, *44* (10), 4001−4006.
(75) Zhang, J.; Liu, G.; Jonas, J. Effects of Confinement on the Glass Transition Temperature of Molecular Liquids. *J. Phys. Chem.* **1992**, *96* (8), 3478−3480.
(76) Askar, S.; Wei, T.; Tan, A. W.; Torkelson, J. M. Molecular Weight Dependence of the Intrinsic Size Effect on Tg in AAO Template-Supported Polymer Nanorods: A DSC Study. *J. Chem. Phys.* **2017**, *146* (20), 203323.
(77) Zhao, H. Y.; Yu, Z. N.; Begum, F.; Hedden, R. C.; Simon, S. L. The Effect of Nanoconfinement on Methyl Methacrylate Polymerization: Tg, Molecular Weight, and Tacticity. *Polymer* **2014**, *55*, 4959−4965.
(78) Zuo, B.; Wang, F.; Hao, Z.; He, H.; Zhang, S.; Priestley, R. D.; Wang, X. Influence of the Interfacial Effect on Polymer Thin-Film Dynamics Scaled by the Distance of Chain Mobility Suppression by the Substrate. *Macromolecules* **2019**, *52*, 3753.
(79) Thees, M. F.; Roth, C. B. Unexpected Molecular Weight Dependence to the Physical Aging of Thin Polystyrene Films Present at Ultra-High Molecular Weights. *J. Polym. Sci., Part B: Polym. Phys.* **2019**, *57* (18), 1224−1238.
(80) Corsi, J. S.; Fu, J.; Wang, Z.; Lee, T.; Ng, A. K.; Detsi, E. Hierarchical Bulk Nanoporous Aluminum for On-Site Generation of Hydrogen by Hydrolysis in Pure Water and Combustion of Solid Fuels. *ACS Sustainable Chem. Eng.* **2019**, *7*, 11194−11204.
(81) Yaghoobnejad Asl, H.; Fu, J.; Kumar, H.; Welborn, S. S.; Shenoy, V. B.; Detsi, E. In Situ Dealloying of Bulk Mg2Sn in Mg-Ion Half Cell as an Effective Route to Nanostructured Sn for High Performance Mg-Ion Battery Anodes. *Chem. Mater.* **2018**, *30* (5), 1815−1824.
(82) Detsi, E.; Cook, J. B.; Lesel, B. K.; Turner, C. L.; Liang, Y. L.; Robbennolt, S.; Tolbert, S. H. Mesoporous Ni60Fe30Mn10-Alloy Based Metal/Metal Oxide Composite Thick Films as Highly Active and Robust Oxygen Evolution Catalysts. *Energy Environ. Sci.* **2016**, *9* (2), 540−549.
(83) Tu, C. H.; Zhou, J.; Doi, M.; Butt, H. J.; Floudas, G. Interfacial Interactions during in Situ Polymer Imbibition in Nanopores. *Phys. Rev. Lett.* **2020**, *125* (12), 127802.
(84) Yao, Y.; Butt, H. J.; Floudas, G.; Zhou, J.; Doi, M. Theory on Capillary Filling of Polymer Melts in Nanopores. *Macromol. Rapid Commun.* **2018**, *39* (14), 1800087.
(85) Schönhals, A.; Goering, H.; Schick, C.; Frick, B.; Zorn, R. Polymers in Nanoconfinement: What Can Be Learned from Relaxation and Scattering Experiments? *J. Non-Cryst. Solids* **2005**, *351* (33−36), 2668−2677.
(86) Detsi, E.; De Jong, E.; Zinchenko, A.; Vuković, Z.; Vuković, I.; Punzhin, S.; Loos, K.; ten Brinke, G.; De Raedt, H.A.; Onck, P.R.; De Hosson, J.T.M. On the Specific Surface Area of Nanoporous Materials. *Acta Mater.* **2011**, *59*, 7488−7497.


https://doi.org/10.1021/acsami.1c12491
*ACS Appl. Mater. Interfaces* XXXX, XXX, XXX−XXX